Chemical Science

ROYAL SOCIETY OF CHEMISTRY

EDGE ARTICLE

View Article Online
View Journal | View Issue

Cite this: *Chem. Sci.*, 2025, **16**, 15546

All publication charges for this article have been paid for by the Royal Society of Chemistry

Aggregation-assisted energy gap modulation controls delayed emission in hybrid charge-transfer emitters†

Kavya Vinod,[a] Najuma Noushad,[a] Hidetoshi Tanaka,[b] Nitha Mohan,[c] Yuya Kokado,[b] Daiki Tomiya,[b] Yasuhiro Kobori[b] and Mahesh Hariharan[*a]

Exploring the impact of molecular aggregation on excited-state energy landscapes is key to tailoring long-lived delayed emission in organic materials. Here, we demonstrate aggregation-assisted energy gap modulation governing the balance between delayed fluorescence (DF) and room-temperature phosphorescence (RTP) in the indole-based hybrid charge-transfer emitters – HD and its brominated analogue BrD. In HD, J-aggregation, facilitated by a collinear molecular arrangement, significantly reduces the singlet–triplet energy gap (ΔE_{ST}), enhances reverse intersystem crossing (RISC), and increases the efficiency of radiative decay from the regenerated singlet state, thereby favouring DF. In contrast, BrD forms H-aggregates through strong π–π interactions, which increase ΔE_{ST}, suppress RISC and stabilize triplet excitons, resulting in prominent RTP. Time-resolved spectroscopy and theoretical calculations reveal that the hybridization of local-excited and charge-transfer states mediates excited-state evolution, with J-aggregation promoting DF and H-aggregation favouring RTP. These results establish a direct link between aggregation and distinct photoluminescence pathways, offering a strategy to tune delayed emission in organic materials.

Received 17th March 2025
Accepted 18th July 2025

DOI: 10.1039/d5sc02071a

rsc.li/chemical-science

Introduction

Photoluminescent organic materials have attracted significant attention due to their diverse optical behaviours.[1–3] Notably, room-temperature phosphorescence (RTP) and delayed fluorescence (DF) have emerged as valuable mechanisms for developing advanced organic materials used in light-emitting diodes, sensors, and bioimaging.[4–9] RTP arises from intersystem crossing (ISC), where excitons undergo a nonradiative spin-flip to the triplet state followed by emission through a sequential spin-forbidden process.[10] In contrast, thermally activated DF arises from the reverse intersystem crossing (RISC) of triplet excitons to the singlet excited state, followed by radiative decay.[11,12] For efficient RISC mediated DF, a small singlet–triplet energy gap (ΔE_{ST}) is essential, while persistent RTP requires mechanisms that stabilize triplet excitons and minimize energy loss through nonradiative pathways.[11] Approaches to enhance RTP include incorporating heavy atoms or heteroatoms to strengthen spin–orbit coupling (SOC) and using rigid molecular frameworks to limit vibrational dissipation.[13–15] In contrast, RISC mediated DF emitters typically feature donor–acceptor structures that spatially separate frontier orbitals, reducing ΔE_{ST}.[16–18] Despite advances in these materials, achieving precise control over excited-state processes to regulate the delayed emission mechanisms remains a significant challenge. Hybrid locally-excited and charge-transfer (HLCT) states offer a promising approach to address this issue.[16,19–22] While charge-transfer (CT) states generally suffer from weak fluorescence due to poor orbital overlap, their low exciton binding energy leads to near-degenerate singlet and triplet states, favouring RISC.[22,23] In contrast, locally excited (LE) states have stronger radiative transitions but a larger ΔE_{ST}, limiting triplet harvesting.[21] By merging LE and CT characteristics into a single HLCT state, it is possible to achieve both efficient luminescence and enhanced exciton utilization.[22]

Beyond molecular design, solid-state organization plays a key role in shaping excited-state properties.[24–27] Unlike doped host–guest matrices where DF is commonly observed, RTP predominantly occurs in crystalline solids where aggregation suppresses nonradiative triplet deactivation.[28,29] Unlike cross-aggregates,[30] J- and H-aggregates strongly influence luminescence pathways,[31,32] yet their role in balancing RTP and DF remains underexplored.[24–26] Recent studies have shown that

[a]*School of Chemistry, Indian Institute of Science Education and Research Thiruvananthapuram (IISER TVM), Maruthamala P. O., Vithura, Thiruvananthapuram 695551, Kerala, India. E-mail: mahesh@iisertvm.ac.in*

[b]*Department of Chemistry, Graduate School of Science, Kobe University, 1-1 Rokkodaicho Nada-ku Kobe, 657-8501, Japan*

[c]*School of Biology, Indian Institute of Science Education and Research Thiruvananthapuram (IISER TVM), Maruthamala P.O., Vithura, Thiruvananthapuram 695551, Kerala, India*

† Electronic supplementary information (ESI) available. CCDC 2429518 and 2429519. For ESI and crystallographic data in CIF or other electronic format see DOI: https://doi.org/10.1039/d5sc02071a

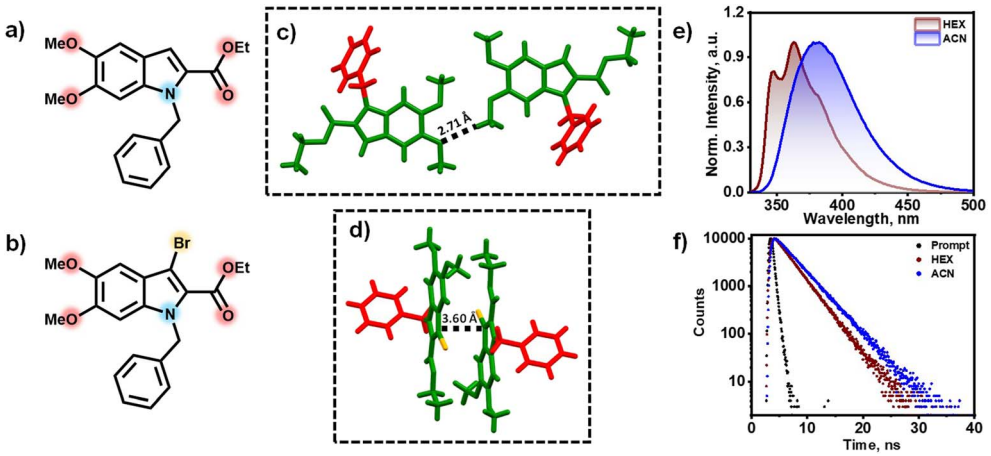

Fig. 1 Chemical structures of (a) HD and (b) BrD; crystal packing of (c) HD and (d) BrD showing the intermolecular distances; (e) normalized fluorescence spectra of HD in HEX and ACN; (f) prompt fluorescence lifetime profile of HD in HEX and ACN.

distinct packing arrangements within molecular polymorphs can lead to concurrent RTP and DF emission, highlighting the importance of aggregate structure in governing excited-state dynamics.[33–39] Energy-gap modulation strategies have also been employed in CT co-crystals to achieve colour-tunable phosphorescence and control RTP/DF output by tuning donor strength and aggregation motifs.[40–43] We investigate how aggregation influences the excited-state properties of two indole-based CT emitters, HD and its brominated analogue BrD (Fig. 1a and b). Both molecules feature a weak donor–acceptor architecture and exhibit a HLCT state. While HD aggregates emit blue delayed fluorescence, BrD aggregates display yellow phosphorescence (Fig. S1†). We observe a correlation between the luminescence behaviour and aggregation pattern. Crystalline HD forms J-aggregates *via* oxygen-centred interactions, reducing ΔE_{ST}, promoting RISC and favouring DF. In contrast, crystalline BrD forms H-aggregates through π–π and Br···H interactions, increasing ΔE_{ST}, suppressing RISC and leading to dominant RTP. Spectroscopic and theoretical analyses establish a direct link between aggregation and delayed emission behaviours, offering a strategy to tune RTP and DF in organic luminescent materials.

Results and discussion

Synthesis, structural characterization and optical properties

Novel indole-based molecules, HD and BrD, were synthesized following synthetic procedures adapted from a previous report.[44] Benzylation of ethyl 5,6-dimethoxy-1*H*-indole-2-carboxylate (DMICE) with benzyl bromide yielded HD in 71% yield (Scheme S1†). Similarly, bromination of DMICE using *N*-bromosuccinimide (NBS), followed by benzylation, produced BrD in 58% yield (Scheme S2†). High-quality, colourless single crystals suitable for X-ray crystallography were obtained by slow evaporation of the indole-based derivatives in ethyl acetate/hexane mixtures at room temperature. The molecular structures of HD and BrD were unequivocally confirmed through single-crystal X-ray diffraction, which also revealed their solid-state packing arrangements (Fig. 1c, d and S2†). HD crystallized in the orthorhombic crystal system with the space group $Pca2_1$, while BrD adopted the monoclinic crystal system with the space group $P2_1/c$ (Table S1†). Dihedral angles of 78° and 79° were observed between the indole unit and the benzyl group in HD and BrD respectively, indicating similar conformational preferences in the solid state. To further validate these findings, geometry optimizations were performed at the cam-b3lyp/6-311+g(d,p) level of theory. The calculated dihedral angles of approximately 72° and 74° for HD and BrD respectively, were in agreement with the experimental values obtained from single-crystal X-ray diffraction (Fig. S3†), supporting the reliability of the computational approach.

The electronic properties of HD and BrD were investigated using UV-vis absorption spectroscopy, fluorescence emission spectroscopy, and time-correlated single-photon counting (TCSPC) measurements. The UV-vis absorption spectrum of HD in hexane (HEX) exhibited a maximum at 303 nm, closely resembling the absorption characteristics of 5,6-dihydroxyindole carboxylic acid (DHICA), which is the monomer of the bio-pigment eumelanin.[45–48] In contrast, the brominated analogue BrD showed a red-shifted absorption maximum at 309 nm in HEX compared to that of HD in HEX, attributed to a reduced HOMO–LUMO gap induced by bromine incorporation (Fig. S4†).[49] Upon photoexcitation, HD in HEX displayed a fluorescence emission maximum at 363 nm, while BrD in HEX exhibited a slightly red-shifted fluorescence maximum at 368 nm (Fig. S4†), corresponding to a bathochromic shift of ~5 nm. Photoluminescence quantum yield measurements in HEX, determined by the relative method, revealed a significant decrease for BrD compared to HD, likely due to the heavy atom effect of bromine.[46] Specifically, HD exhibited a photoluminescence quantum yield (ϕ_f) of 52.0% in HEX, which dropped to 1.9% for BrD in HEX, highlighting the pronounced impact of bromine substitution on emission efficiency.[50]

To explore solvent effects, the steady-state UV-vis absorption and fluorescence spectra of HD and BrD were recorded in two solvents of different dielectric constants, *i.e.*, HEX ($\varepsilon = 1.88$) and

acetonitrile (ACN, $\varepsilon = 37.5$). The UV-vis absorption spectra of both compounds showed minimal solvent dependence, indicating that the $S_0 \rightarrow S_1$ transition is dominated by an LE state with negligible solvent sensitivity (Fig. S5†). In contrast, the fluorescence spectra exhibited significant solvent-dependent changes. In nonpolar HEX, the emission spectra of HD and BrD displayed well-resolved vibronic features, whereas in polar ACN, the spectra broadened and red-shifted, suggesting the emergence of HLCT character in the relaxed S_1 state (Fig. 1e and S6†).[21] In both HD and BrD, the HLCT state likely arises from the interplay and coupling between LE and CT states. As solvent polarity increases, the CT energy level decreases due to stabilization from stronger solvent interactions, while the LE state remains largely unchanged.[22] In low-polarity solvents, luminescence is primarily governed by the LE component, as indicated by the vibronically resolved emission band. With increasing polarity, the lower-energy CT component progressively influences the emission process, leading to an intercrossed HLCT character.

Solvent polarity also affected the fluorescence lifetimes of HD and BrD. In nonpolar HEX, HD showed a mono-exponential decay with a 2.8 ns lifetime, which increased to 3.4 ns in polar ACN, consistent with HLCT emission (Fig. 1f). The mono-exponential behaviour suggests that LE and CT states merge into a single hybridized state.[22] This state likely combines the large dipole moment of the CT state with the strong orbital overlap of the LE state, resulting in high emission. BrD in HEX showed an average fluorescence decay of <1 ns. Meanwhile in ACN, BrD showed a mono-exponential fluorescence lifetime of 3.4 ns (Fig. S7†). The mono-exponential and increased fluorescence lifetimes in polar solvents for HD and BrD reflect the influence of solvation and the radiative nature of the excited-state hybrid charge-transfer process.[21] The excited-state electronic configuration further confirms the HLCT nature of emission in HD and BrD, involving electron density redistribution between the indole ring and the benzyl unit (Fig. 2e, S8, Tables S2 and S3†), unlike their non-benzylated analogues, where both hole and electron densities remain confined only to the indole moiety (Fig. S9†).

The UV-vis absorption and emission spectra of HD and BrD in the crystalline state are presented in Fig. S10.† Significant differences between the solution and crystalline spectra of HD and BrD highlight the impact of aggregation.[51] In the crystalline state, HD exhibited a broadened absorption band extending up to 390 nm, with a tail reaching 400 nm, indicative of strong intermolecular interactions. For crystalline BrD, the absorption spectrum showed even greater broadening and a pronounced red shift, with prominent absorption up to 400 nm. Fluorescence emission spectra in the crystalline state revealed maxima at 382 nm for HD and 392 nm for BrD (Fig. S10†). The substantial red shifts in the electronic absorption spectra of the crystalline assemblies compared to their monomeric forms suggest excitonic interactions. Additionally, crystalline BrD exhibited a weak, red-shifted emission band at 475–650 nm, which we attribute to triplet-state emission, consistent with previous studies on modified indole molecules.[50] Photoluminescence quantum yield measurements in the crystalline state, determined using the absolute method, yielded values of 21.3% for HD and 0.18% for BrD.

To elucidate how structural motifs govern excited-state behaviour,[52] we analysed the crystal packing of the benzylated indole molecules HD and BrD, identifying their dominant dimeric arrangements (Fig. S11†). In HD, close intermolecular contacts are dominated by H···H interactions, as revealed by Hirshfeld surface analysis, which shows that these account for 51.4% of the total intermolecular contacts (Fig. S12 and Table S4†). A distinctive tail-to-tail dimeric configuration stabilized by CH···O contacts was observed in HD. In contrast, BrD features additional stabilizing contacts, including Br···H (10.9%) and C···C (3.3%) interactions (Fig. S13 and Table S4†). Notably, the C···C contacts in BrD facilitate π–π stacking with an intermolecular distance of 3.60 Å, forming a stacked dimeric assembly absent in HD (Fig. 1d). To quantify the stabilizing forces in these aggregates, symmetry-adapted perturbation theory (SAPT(0)) calculations were performed on the dimers,[53] revealing dispersion interactions as the primary contributor for the tail-to-tail dimer in HD and π–π stacked dimer in BrD (Table S5†). Non-covalent interaction (NCI) index analysis and electrostatic potential (ESP) maps further corroborated these findings, indicating strong stabilization within both dimer assemblies (Fig. S14 and S15†).[54,55]

Aggregation behaviour was further investigated in THF/H_2O mixtures. Decreasing the f_{THF} percent (f_{THF} is the fraction of THF in the total volume of solution) led to changes in the fluorescence emission of HD and BrD aggregates. For HD, the fluorescence intensity red-shifted from 373 nm in 100% THF to 413 nm in 10% THF (Fig. S16†). On the other hand, BrD exhibited an additional band appearing at 470–650 nm in 10% THF compared to the sharp emission band centred at 377 nm in 100% THF. The fluorescence intensity of BrD aggregates at 360–450 nm decreased by ~8.5 times in 10% THF solutions with respect to 100% THF solutions (Fig. S17†). These results demonstrate that aggregation significantly alters the photophysical properties of HD and BrD, modulating their decay pathways in the solution state. The spectral shifts and emission behaviour in THF/water mixtures closely parallel those observed in the crystalline state, indicating that solution-state aggregates can emulate solid-state electronic interactions.

Delayed emission in monomer *versus* aggregates

To elucidate the differences in excited-state behaviour among monomeric solutions, aggregate solutions, and crystalline states, gated-emission experiments were conducted. At room temperature, crystalline HD exhibited a strong, well-defined delayed emission peak at 387 nm with a lifetime of 484 μs upon 340 nm excitation (Fig. 2a and b). This peak closely aligns with the prompt crystalline emission, suggesting DF originating from the singlet excited state ($S_1 \rightarrow S_0$). Temperature-dependent gated emission measurements further confirmed the role of thermal energy in activating the DF (Fig. S18†): at 77 K, the delayed emission intensity and lifetime significantly decreased, with the emergence of a vibronically resolved red-shifted band (480–650 nm), attributed to triplet-state emission

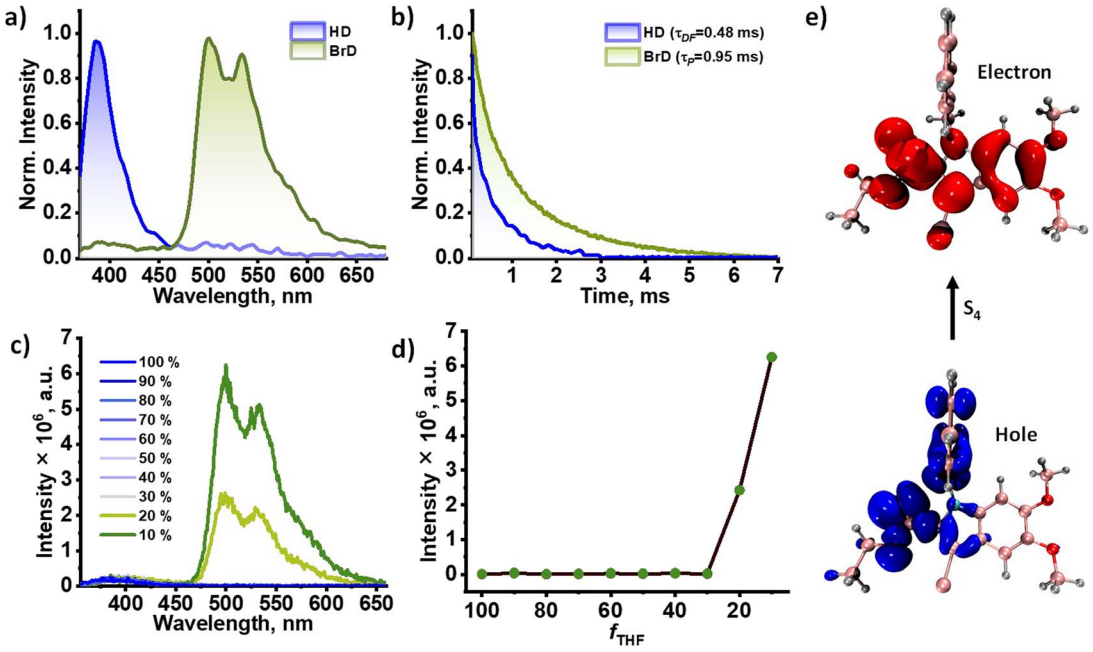

Fig. 2 a) Normalized gated emission spectra of crystalline HD and BrD at room temperature (delay = 0.05 ms); (b) decay profiles of gated emission of crystalline HD and BrD; (c) gated emission spectra of BrD aggregates in different % of THF concentration (f_{THF}) in THF-water mixtures at room temperature (delay = 0.05 ms); (d) plot showing emergence of RTP (λ_{em} = 500 nm) with increase in f_{THF}; (e) singlet excited state of BrD showing partially delocalized hole and electron densities.

($T_1 \rightarrow S_0$). This behaviour indicates that thermal energy is essential for efficient RISC in HD, a hallmark of RISC mediated DF materials.[5] To exclude the possibility of triplet–triplet annihilation (TTA), we examined the excitation power dependence of the delayed emission lifetimes. The observed invariance in lifetime across different excitation intensities supports a monomolecular RISC pathway (Fig. S19†). This is consistent with recent studies reporting efficient RISC in CT systems, even in the presence of relatively large S_1–T_1 energy gaps.[24,56] In solution, HD displayed weak DF with a lifetime of <10 μs, suggesting that aggregation provides a rigid environment and enhances RISC, facilitating upconversion to the CT state (Fig. S20†).[25] In contrast, crystalline BrD exhibited pronounced RTP, with a strong phosphorescence band spanning 480–650 nm and a lifetime of 950 μs (Fig. 2a and b). A weaker DF band (370–450 nm) was also observed. The phosphorescence intensity was nearly 15 times greater than the DF, highlighting efficient triplet-state emission. The presence of bromine in BrD likely influences the dominance of phosphorescence by enhancing ISC, while crystallization favours radiative decay over nonradiative relaxation from the lowest triplet state.[28,57] In solution, BrD primarily emits *via* fluorescence at 360–440 nm at room temperature, but at 77 K, a distinct phosphorescence band (460–660 nm) emerged, with an intensity ~22 times greater than fluorescence intensity and a lifetime of 19.3 ms (Fig. S21†). The temperature dependence confirms the phosphorescent nature of the emission, with bromine facilitating the ISC. Crystallization further stabilizes triplet excitons by suppressing nonradiative decay and minimizing oxygen quenching, demonstrating the critical role of molecular packing in modulating excited-state dynamics (*vide infra*).[28]

To mimic interchromophore interactions and the rigid crystalline environment in solution, delayed emission measurements were performed for HD and BrD in THF/water mixtures. For HD, decreasing the THF fraction (f_{THF}) significantly altered the DF intensity, with a 3-fold increase at f_{THF} = 10% compared to f_{THF} = 100% (Fig. S22†). The DF lifetime of HD increased from >10 μs in f_{THF} = 100% to 0.15 ms in f_{THF} = 10% solutions. This suggests that aggregation induces rigidity within the chromophores, promoting RISC, even within solution-states.[56] For BrD, phosphorescence emerged in solutions where f_{THF} = 20% and further intensified as f_{THF} decreased (Fig. 2c and d). At f_{THF} = 10%, the phosphorescence intensity was ~25 times greater than the fluorescence at 385 nm, with lifetimes extending from 0.55 ms (f_{THF} = 20%) to 0.75 ms (f_{THF} = 10%), indicative of aggregation-induced phosphorescence (Fig. S23†). Incorporating HD and BrD into poly(methyl methacrylate) (PMMA) matrix resulted in delayed emission lifetimes that were shorter than those observed in the crystalline state, though still significantly longer than in neat aggregate (f_{THF} = 100%) solutions. PMMA-coated thin films of HD exhibited DF at 385 nm with a lifetime <10 μs, while BrD films showed intense phosphorescence (470–650 nm) with a lifetime of 0.08 ms (Fig. S24†). Although the PMMA matrix acts as an oxygen barrier and suppresses quenching, the delayed emission lifetimes were reduced compared to the crystalline state, likely due to differences in molecular packing and rigidity.[56] This suggests that while PMMA can stabilize triplet excitons to some extent, the highly ordered crystalline environment provides superior stabilization for long-lived delayed emission.[58] Nevertheless, the PMMA films successfully replicated the key photophysical features of the crystalline state, demonstrating the

potential of polymer matrices to mimic solid-state behaviour in thin-film applications. The ability to replicate crystalline electronic interactions and rigid environments in solution-state aggregates and polymer matrices establishes a versatile platform for manipulating photophysical behaviour, bridging the gap between solution and solid-state properties.

Excited state deactivation

To investigate the excited-state processes responsible for efficient delayed emission in the indole-based molecules HD and BrD, femtosecond transient absorption (fsTA) measurements were performed. The fsTA spectra of HD and BrD in THF are presented in Fig. 3. For HD, photoexcitation at 330 nm using a 100-fs pump pulse generated a broad positive feature spanning 470–740 nm, resembling the singlet absorption observed in DHICA and its protected derivatives.[45,50,59] Within few tens of picoseconds, the absorption maximum red-shifted from 600 nm to 660 nm, and the resulting species persisted throughout the experimental time window of ~3.5 ns. Global fitting of the time-resolved fsTA spectra using an A → B → GS (GS = ground state) sequential model yielded the evolution-associated spectra (EAS) for HD. Deconvolution of the fsTA spectra of HD in THF revealed two spectral components. The first component (component A), attributed to the relaxation of the singlet excited state, decayed with a lifetime of 63.7 ps. The second component (component B), corresponding to the HLCT state, decayed within 3.66 ns, closely matching the fluorescence lifetime. Additionally, a marginal rise at ~460 nm was observed for HD at time delays >3.5 ns, which, based on previous studies of modified indoles, could reveal the triplet state evolution from the HLCT state.[50]

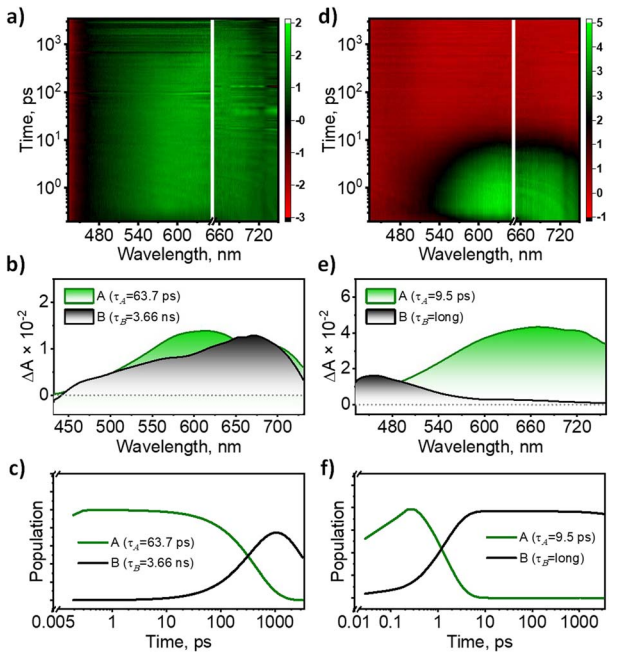

Fig. 3 (a) Femtosecond transient absorption (fsTA) contour plot of HD in THF (colour scale of the contour plot represents ΔA/10^2 a.u.), (b) deconvoluted EAS plot of HD in THF, (c) deconvoluted decay time constants of the EAS for HD in THF; (d) FsTA contour plot of BrD in THF, (e) deconvoluted EAS plot of BrD in THF, (f) deconvoluted decay time constants of the EAS for BrD in THF.

For BrD in THF, excitation at 330 nm produced a broad singlet absorption feature between 510–740 nm, peaking at 665 nm (Fig. 3d). The decay of the singlet excited state within a few picoseconds was accompanied by the emergence of a peak at ~460 nm. Unlike HD, the initial broad feature at 600 nm was not observed for BrD, likely due to faster CT dynamics. Given that ISC occurs within a few picoseconds, solvent relaxation of the Frenkel exciton state may occur on a timescale comparable to or faster than the instrument's response function. Global fitting of the fsTA spectra of BrD using the A → B → GS model yielded two spectrally distinct components (Fig. 3e). The first component (component A), representing the decay of the HLCT state, exhibited a lifetime of 9.5 ps, while the second component (component B), attributed to triplet states, persisted throughout the experimental time delay (>3.5 ns).[50] The CT and ISC dynamics of HD and BrD mediate the delayed emission pathways observed for the molecules. The distinct spectral evolution and lifetimes of the HLCT and triplet states provide critical insights into the photophysical mechanisms underlying delayed emission in these modified indoles.[60] The benzyl groups in HD and BrD introduce low-energy CT states that hybridize with the main indole unit's singlet $^1(\pi–\pi^*)$ state. These HLCT states comprise a partially localized electron cloud across the indole backbone and benzyl ring, reducing the exchange energy and promoting triplet formation in both compounds. Furthermore, in BrD, bromine accelerates intersystem crossing (ISC) and yields efficient triplet-state population. In contrast, HD exhibits a long-lived CT state that facilitates RISC from the triplet excited state back to the emissive HLCT state, enabling DF.

Given the efficient DF and RTP observed in crystalline and polymer-coated films of HD and BrD, fsTA measurements were extended to concentrated thin films of HD and BrD embedded in PMMA matrices. The excited-state absorption peaks of these aggregated films exhibited subtle deviations from solution-phase peaks, likely due to perturbations in excited-state energetics induced by molecular aggregation.[61] For HD film, photoexcitation at 330 nm generated an excited-state absorption band with a maximum at 575 nm (Fig. S25†). Within a few picoseconds, the spectral intensity diminished, and a broader species developed at ~440–700 nm. Spectral deconvolution revealed three components in the fsTA spectra. The first component (component A), associated with the singlet excited state, decayed within 4.9 ps to form component B. Component B is noteworthy due to its broadened characteristic and is attributed to the HLCT state. The HLCT state decayed within 113.8 ps to form a relaxed HLCT state with significant absorption in 440 nm range.[46,50] The relaxed HLCT state persisted even at time delays greater than 3.5 ns. For BrD, the excited-state dynamics were significantly faster than those of HD (Fig. S26†). Photoexcitation initially produced an excited-state absorption band at 575 nm, which decayed within a few hundred femtoseconds to form a broad HLCT band. The population of triplet states was observed upon the decay of the broad HLCT state. Spectral deconvolution identified the singlet

excited state (component A) with a lifetime of 1.9 ps, followed by the HLCT state (component B) with a decay time constant of 69.0 ps. Triplet excited states (component C) evolved with the decay of HLCT state and persisted for >3.5 ns. In both HD and BrD thin film aggregates, ultrafast population of intermediate HLCT and triplet states as well as rigidification suppresses nonradiative internal conversion and vibronic relaxation, thereby enhancing delayed emission efficacy.

Time-resolved electron paramagnetic resonance (TR-EPR) measurements in crystalline HD and BrD further confirmed the triplet excited state populations in the crystalline samples. After photoexcitation at 355 nm by a nanosecond pulsed laser, a TR-EPR spectrum was observed with an electron spin polarization (ESP) pattern of E/E/E/A/A/A for both samples at 80 K, where A and E represent enhanced absorptive and emissive polarizations, respectively (Fig. S27†). The triplet states exhibit zero-field-splitting (ZFS) simulated by the parameters of $(D, E) = (0.107\ \mathrm{cm}^{-1}, -0.015\ \mathrm{cm}^{-1})$ for HD and $(0.107\ \mathrm{cm}^{-1}, -0.035\ \mathrm{cm}^{-1})$ for BrD considering the relative sublevel populations by ISC of $(P_x, P_y, P_z) = (0.5, 0.5, 0)$ for both samples. The EPR parameters are typical of the $^3(\pi\text{–}\pi^*)$ characters of the metal-free aromatic molecules, denoting that the in-plane sublevel populations occurs *via* the spin–orbit coupling through the vibronic effect between the $^1(\pi\text{–}\pi^*)$ and $^3(\pi\text{–}\pi^*)$ characters, while smaller magnitudes of the parameters of $|D|$ ($<0.05\ \mathrm{cm}^{-1}$) are reported for the ^{3}CT characters.[62–64] The observed triplet characters are consistent with the formation of low-lying T_1 states with $^3(\pi\text{–}\pi^*)$ character, stabilized by spin–spin exchange, as supported by DFT calculations (Fig. S28†).[65]

Our investigation provided fresh insights into the mechanisms governing delayed emission in these systems. In BrD aggregates, the energy levels were relatively well separated so that the initially excited singlet state predominantly evolved into HLCT states, which then efficiently generated lower-energy triplet excited states. These processes were strongly influenced by intermolecular interactions and the rigid constraints of the solid state, resulting in an alternative pathway for triplet exciton decay rather than efficient RISC.[60] On the other hand, HD aggregates displayed significant excited-state mixing due to the small singlet–triplet energy gap: a transient CT state rapidly relaxed into a lower-energy configuration with significant triplet mixing. The small energetic gap between the CT and higher triplet excited states enabled robust mixing, as suggested by correlated transient absorption features.[60] The nature of this CT-triplet mixture evolved over time, evidenced by the persistence of the relaxed HLCT absorption even at time delays greater than 3.5 ns. In HD, reverse internal conversion from the localized T_1 state to higher-lying HLCT triplet states could be facilitated. Further, a spin-flip transition to the ^{1}CT configuration could be enabled, which subsequently relaxes radiatively *via* mixing with the $^1(\pi\text{–}\pi^*)$ state. These findings are consistent with recent studies on small π-conjugated DF systems, which emphasize that a substantial CT contribution and close energetic proximity to a T_n state, can significantly enhance RISC.[66,67] A detailed analysis of the aggregate structures of HD and BrD, presented in the following section, elucidates why crystalline samples exhibit efficient delayed emission compared to their respective solution counterparts.

Influence of interchromophore interactions on delayed emission

Exciton coupling within the dimeric assemblies directly influence the difference in photophysical properties of HD and BrD crystals (Table S6†). Exciton splitting arises from long-range coulombic coupling (J_{Coul}) and short-range CT coupling (J_{CT}) mediated by HOMO–LUMO overlaps (Fig. S29†).[52] For HD, electronic coupling calculations revealed a J_{Total} of $-142\ \mathrm{cm}^{-1}$, characteristic of J-aggregate behaviour dominated by coulombic interactions.[68] This J-type coupling aligns with the observed red-shifted, narrow absorption band in the crystalline state (Fig. S10†), as head-to-tail transition dipole alignment decreases energy of the allowed transition. On the other hand, BrD demonstrated $J_{\mathrm{Total}} = 213\ \mathrm{cm}^{-1}$, reflecting H-aggregate behaviour with significant contributions from both coulombic and orbital overlap interactions. The absorption broadening in the blue-wavelength region for BrD crystals arises from face-to-face π-stacking, which increases the energy of the allowed excitonic state, which is a hallmark of H-aggregates (Fig. S10†).[68] Transition dipole moment analyses confirmed the aggregation patterns in HD and BrD (Fig. S30†).

Excited-state energy calculations on crystallographic dimers further underscored the role of aggregation in modulating excited-state pathways (Fig. 4). In HD, the dimeric $S_0 \rightarrow S_1$ transition exhibited a significant oscillator strength ($f = 0.15$) which is characteristic of J-aggregation.[52,68] Notably, while the HD monomer displayed an extremely small singlet–triplet energy gap ($\Delta E_{\mathrm{ST}} = 0.003$ eV), aggregation tuned this gap to $\Delta E_{\mathrm{ST}} = -0.003$ eV (Tables S7 and S8†). This near-zero, marginally negative energy gap facilitates efficient RISC from T_n to S_1, following reverse internal conversion from T_1, thereby enabling and supporting the observed delayed fluorescence in HD aggregates.[24] In contrast, the $S_0 \rightarrow S_1$ transition in BrD aggregates exhibited near-zero oscillator strength, contrasting sharply with the monomer's value ($f = 0.31$), which is indicative of H-aggregation. As a result, the $S_0 \rightarrow S_2$ transition emerged as the first bright state. Moreover, for monomeric BrD, the ΔE_{ST} was 0.047 eV, which increased to 0.77 eV upon aggregation (Tables S9 and S10†). Although crystallization-induced rigidity and the presence of bromine can suppress nonradiative decay and enhance ISC, these factors alone do not account for the observed RTP in BrD. Notably, previously reported brominated, non-benzylated indole-based analogues did not exhibit RTP in the crystalline state, despite comparable heavy-atom substitution and packing-induced rigidity.[46,50] H-aggregation, which favours strong π–π stacking, typically promotes ISC and the stabilization of triplet states, directing the system toward RTP rather than DF.

In both HD and BrD aggregates, the number of high-lying triplet excited states increases (Fig. 4), suggesting that crystalline packing facilitates additional ISC pathways compared to solution. To account for the stark contrast between the DF observed in HD crystals and the RTP in BrD crystals, the

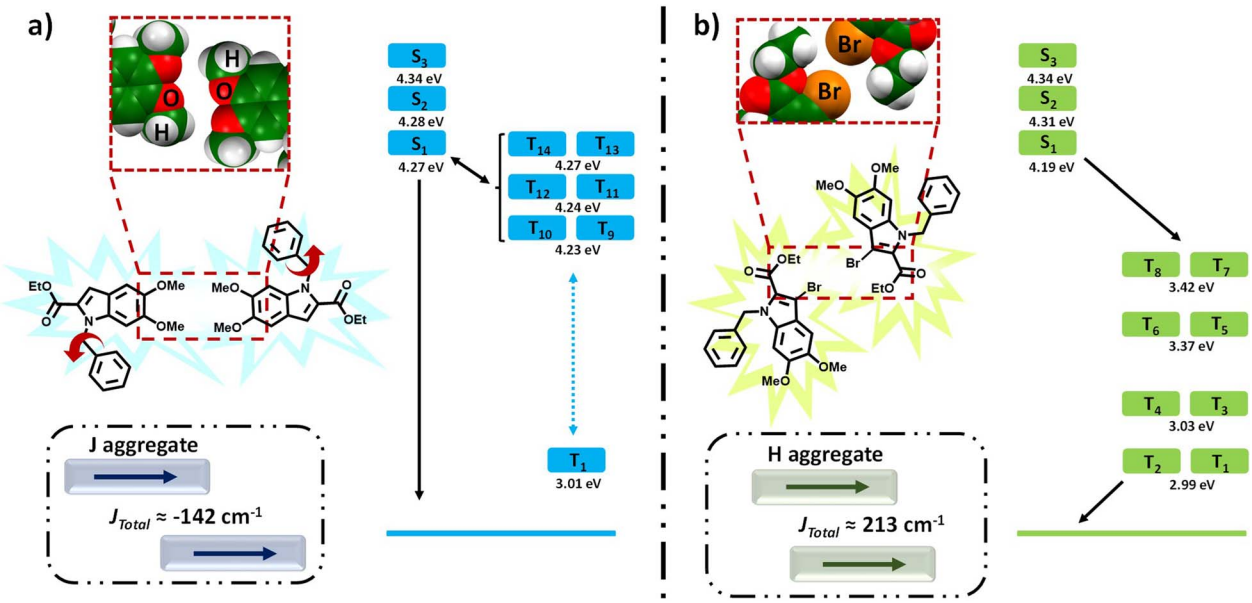

Fig. 4 (a) In crystalline state, HD molecules are arranged as a oxygen-centred J-type aggregate with reduced singlet–triplet energy gap, enabling DF; (b) in crystalline state, BrD molecules are arranged as a π–π-stacked H-type aggregate with increased singlet–triplet energy gap, disabling DF and promoting RTP. The navy blue and olive green arrows denote the transition dipole moments for the S_1 transition in J-aggregates of HD and S_2 transition in H-aggregates of BrD respectively.

emission oscillator strength of the S_1 state also emerges as a key distinction factor. As supported by the excited state energy calculations (Tables S7–S10†), the oscillator strength of S_1 state is substantially larger in the HD dimer than in the BrD dimer. This difference indicates more efficient radiative decay in HD ($k_{r,f} \approx 1.21 \times 10^8$ s^{-1}) and notably suppressed radiative decay in BrD ($k_{r,f} \approx 7.61 \times 10^4$ s^{-1}), according to Einstein's expression for spontaneous emission, $k_{r,f} = fE_g^2/1.499$, where E_g is the energy of S_1 state and f is the oscillator strength, highlighting the crucial role of aggregation in tuning emission properties. Although the oscillator strength (f) of the S_1 state increases upon aggregation in crystalline HD, the photoluminescence quantum yield decreases in comparison to solution, owing to the emergence of closely spaced triplet states that introduce additional ISC pathways competing with radiative decay.

The excited-state energy landscape in crystalline HD and BrD offers key insights into their divergent emission behaviours. In HD aggregates, although higher triplet states such as T_{13} and T_{14} are nearly isoenergetic with S_1, delayed fluorescence occurs due to a thermally assisted, multistep RISC mechanism rather than direct RISC from these higher states. Transient absorption spectroscopy suggests that the T_n states exhibit HLCT character, while time-resolved EPR measurements identify T_1 as a localized $^3(\pi$–$\pi^*)$ state. These results, together with temperature-dependent gated emission, support that excitons initially relax to T_1, followed by vibrationally activated upconversion to higher-lying T_n states, which then undergo RISC to S_1.[67,69–72] Importantly, the distinct electronic characters of T_1 (LE) and T_n (HLCT) enable non-adiabatic coupling, facilitating efficient RISC through a $T_1 \rightarrow T_n \rightarrow S_1$ pathway. The absence of strong π–π interactions around the benzyl substituents in HD may enable low-frequency torsional modes, which can couple to phonon modes in the aggregate to compensate the activation enthalpy-entropy to assist the upconversion.[73] In contrast, BrD aggregates exhibit neither near-resonant T_n states nor structural flexibility around the benzyl groups (Fig. S31†). The presence of strong π–π stacking interactions in BrD constrains molecular motion and restricts access to thermally driven pathways. Additionally, the narrower triplet manifold (T_n–$T_1 \sim 0.43$ eV) facilitates rapid internal conversion, precluding repopulation of T_n and suppressing RISC. Collectively, these findings illustrate how molecular packing modulated the excited-state dynamics: J-aggregates, as observed in HD, lowered ΔE_{ST} and enhanced RISC to favour DF, while H-aggregates in BrD increased ΔE_{ST} and suppressed RISC, channelling excitation energy into phosphorescence.

Conclusions

The present work demonstrates how molecular aggregation in HLCT systems can effectively modulate the energy gap between singlet and triplet states, enabling a tunable transition between the DF and RTP. By leveraging J-aggregation in an indole-based molecule (HD) and H-aggregation in its brominated derivative (BrD), we show that the interplay between oxygen-centred and bromine-induced interactions can significantly influence the excited-state dynamics, ultimately steering the emission pathway toward DF or RTP. The HLCT state integrates the orbital overlap of LE states with the dipolar character of CT states, enabling efficient radiative decay in crystalline HD. Gated emission measurements reveal that the phosphorescence lifetime for crystalline BrD is 0.95 ms, while the DF lifetime for crystalline HD is 0.48 ms, both at room temperature, underscoring the efficiency of the long-lived emission channels for

both systems. Solution-phase aggregation of HD and BrD is achieved in THF/H_2O mixtures, where the DF lifetime for HD aggregates is 0.15 ms, while the RTP lifetime for BrD aggregates is 0.75 ms in 10% THF solutions. The hybrid CT states play a central role in mediating the excited-state evolution, with aggregation type (J-*versus* H-aggregate) deciphering the delayed emission mechanisms (DF *versus* RTP) in HD and BrD. Our findings highlight the importance of aggregation-assisted energy gap modulation in achieving long-lived, efficient emission in organic luminescent materials. Furthermore, the work presents new opportunities for controlling emission behaviour in solid-state materials, bridging the gap between solution and solid-state properties for practical applications.

Data availability

All experimental procedures and characterization data are available in the ESI.†

Author contributions

All authors have contributed to the final version of the manuscript.

Conflicts of interest

The authors declare no conflicts of interest.

Acknowledgements

M. H. acknowledges the Science and Engineering Research Board (CRG/2023/005859), Department of Science and Technology, Govt. of India, for financial support. K. V. acknowledges CSIR for financial assistance. N. N. acknowledges IISER TVM for financial support. This work was partially supported by JSPS KAKENHI JP25H00903 and the JST-CREST Program (JPMJCR23I6). We thank Mr Alex Andrews P. for his support with the SC-XRD analyses. We thank the Padmanabha HPC cluster at IISER TVM for the computing facility.

References

1 R. Kabe and C. Adachi, *Nature*, 2017, **550**, 384–387.
2 Y. Li, M. Gecevicius and J. Qiu, *Chem. Soc. Rev.*, 2016, **45**, 2090–2136.
3 B. Zhou and D. Yan, *Adv. Funct. Mater.*, 2019, **29**, 1807599.
4 C. Si, T. Wang, A. K. Gupta, D. B. Cordes, A. M. Z. Slawin, J. S. Siegel and E. Zysman-Colman, *Angew. Chem., Int. Ed.*, 2023, **62**, e202309718.
5 K.-H. Kim and J.-J. Kim, *Adv. Mater.*, 2018, **30**, 1705600.
6 J. U. Kim, I. S. Park, C.-Y. Chan, M. Tanaka, Y. Tsuchiya, H. Nakanotani and C. Adachi, *Nat. Commun.*, 2020, **11**, 1765.
7 X. Li, G. Baryshnikov, C. Deng, X. Bao, B. Wu, Y. Zhou, H. Ågren and L. Zhu, *Nat. Commun.*, 2019, **10**, 731.
8 K. Y. Zhang, Q. Yu, H. Wei, S. Liu, Q. Zhao and W. Huang, *Chem. Rev.*, 2018, **118**, 1770–1839.
9 Y. Yang, Y. Liang, Y. Zheng, J.-A. Li, S. Wu, H. Zhang, T. Huang, S. Luo, C. Liu, G. Shi, F. Sun, Z. Chi and B. Xu, *Angew. Chem., Int. Ed.*, 2022, **61**, e202201820.
10 Y. Zhao, J. Yang, C. Liang, Z. Wang, Y. Zhang, G. Li, J. Qu, X. Wang, Y. Zhang, P. Sun, J. Shi, B. Tong, H.-Y. Xie, Z. Cai and Y. Dong, *Angew. Chem., Int. Ed.*, 2024, **63**, e202317431.
11 J. M. Dos Santos, D. Hall, B. Basumatary, M. Bryden, D. Chen, P. Choudhary, T. Comerford, E. Crovini, A. Danos, J. De, S. Diesing, M. Fatahi, M. Griffin, A. K. Gupta, H. Hafeez, L. Hämmerling, E. Hanover, J. Haug, T. Heil, D. Karthik, S. Kumar, O. Lee, H. Li, F. Lucas, C. F. R. Mackenzie, A. Mariko, T. Matulaitis, F. Millward, Y. Olivier, Q. Qi, I. D. W. Samuel, N. Sharma, C. Si, L. Spierling, P. Sudhakar, D. Sun, E. Tankelevičiūtė, M. Duarte Tonet, J. Wang, T. Wang, S. Wu, Y. Xu, L. Zhang and E. Zysman-Colman, *Chem. Rev.*, 2024, **124**, 13736–14110.
12 R. Okumura, H. Tanaka, K. Shizu, S. Fukushima, Y. Yasuda and H. Kaji, *Angew. Chem., Int. Ed.*, 2024, **63**, e202409670.
13 W. Zhao, Z. He and B. Z. Tang, *Nat. Rev. Mater.*, 2020, **5**, 869–885.
14 Kenry, C. Chen and B. Liu, *Nat. Commun.*, 2019, **10**, 2111.
15 M. A. Niyas, S. Garain, K. Shoyama and F. Würthner, *Angew. Chem., Int. Ed.*, 2024, **63**, e202406353.
16 D. Chen, H. Wang, D. Sun, S. Wu, K. Wang, X.-H. Zhang and E. Zysman-Colman, *Adv. Mater.*, 2024, **36**, 2412761.
17 S. Garain, S. M. Wagalgave, A. A. Kongasseri, B. C. Garain, S. N. Ansari, G. Sardar, D. Kabra, S. K. Pati and S. J. George, *J. Am. Chem. Soc.*, 2022, **144**, 10854–10861.
18 D. G. Congrave, B. H. Drummond, P. J. Conaghan, H. Francis, S. T. E. Jones, C. P. Grey, N. C. Greenham, D. Credgington and H. Bronstein, *J. Am. Chem. Soc.*, 2019, **141**, 18390–18394.
19 L. Chen, S. Zhang, H. Li, R. Chen, L. Jin, K. Yuan, H. Li, P. Lu, B. Yang and W. Huang, *J. Phys. Chem. Lett.*, 2018, **9**, 5240–5245.
20 G. Meng, H. Dai, Q. Wang, J. Zhou, T. Fan, X. Zeng, X. Wang, Y. Zhang, D. Yang, D. Ma, D. Zhang and L. Duan, *Nat. Commun.*, 2023, **14**, 2394.
21 C. Liao, S. Wang, B. Chen, Q. Xie, J. Feng, J. Bai, X. Li and H. Liu, *Angew. Chem., Int. Ed.*, 2025, **64**, e202414905.
22 W. Li, Y. Pan, R. Xiao, Q. Peng, S. Zhang, D. Ma, F. Li, F. Shen, Y. Wang, B. Yang and Y. Ma, *Adv. Funct. Mater.*, 2014, **24**, 1609–1614.
23 D. Aumiler, S. Wang, X. Chen and A. Xia, *J. Am. Chem. Soc.*, 2009, **131**, 5742–5743.
24 S. Li, L. Fu, X. Xiao, H. Geng, Q. Liao, Y. Liao and H. Fu, *Angew. Chem., Int. Ed.*, 2021, **60**, 18059–18064.
25 H. Tsujimoto, D.-G. Ha, G. Markopoulos, H. S. Chae, M. A. Baldo and T. M. Swager, *J. Am. Chem. Soc.*, 2017, **139**, 4894–4900.
26 H. Gong, Y. Song, J. He, P. Wang, Y. Xiang, S. Li, J. Yao, B. Liao, Q. Liao and H. Fu, *Angew. Chem., Int. Ed.*, 2024, **63**, e202400089.
27 L.-Y. Hsu, S. Maity, Y. Matsunaga, Y.-F. Hsu, Y.-H. Liu, S.-M. Peng, T. Shinmyozu and J.-S. Yang, *Chem. Sci.*, 2018, **9**, 8990–9001.

28 O. Bolton, K. Lee, H.-J. Kim, K. Y. Lin and J. Kim, *Nat. Chem.*, 2011, **3**, 205–210.
29 K. Stavrou, L. G. Franca and A. P. Monkman, *ACS Appl. Electron. Mater.*, 2020, **2**, 2868–2881.
30 E. Sebastian, A. M. Philip, A. Benny and M. Hariharan, *Angew. Chem., Int. Ed.*, 2018, **57**, 15696–15701.
31 E. E. Greciano, J. Calbo, E. Ortí and L. Sánchez, *Angew. Chem., Int. Ed.*, 2020, **59**, 17517–17524.
32 R. Manha Veedu, N. Niemeyer, N. Bäumer, K. Kartha Kalathil, J. Neugebauer and G. Fernández, *Angew. Chem., Int. Ed.*, 2023, **62**, e202314211.
33 J. Xue, Q. Liang, R. Wang, J. Hou, W. Li, Q. Peng, Z. Shuai and J. Qiao, *Adv. Mater.*, 2019, **31**, 1808242.
34 E. Lucenti, A. Forni, C. Botta, L. Carlucci, C. Giannini, D. Marinotto, A. Previtali, S. Righetto and E. Cariati, *J. Phys. Chem. Lett.*, 2017, **8**, 1894–1898.
35 J. Gierschner, L. Lüer, B. Milián-Medina, D. Oelkrug and H.-J. Egelhaaf, *J. Phys. Chem. Lett.*, 2013, **4**, 2686–2697.
36 S. Xu, T. Liu, Y. Mu, Y.-F. Wang, Z. Chi, C.-C. Lo, S. Liu, Y. Zhang, A. Lien and J. Xu, *Angew. Chem., Int. Ed.*, 2015, **54**, 874–878.
37 S. Li, J. Chen, Y. Wei, J. De, H. Geng, Q. Liao, R. Chen and H. Fu, *Angew. Chem., Int. Ed.*, 2022, **61**, e202209211.
38 L. Jin, Z. Wang, W. Mo, H. Deng, W. Hong and Z. Chi, *Angew. Chem., Int. Ed.*, 2024, **63**, e202410974.
39 T. Okamoto, S. Izawa, M. Hiramoto and Y. Kobori, *J. Phys. Chem. Lett.*, 2024, **15**, 2966–2975.
40 S. Garain, S. N. Ansari, A. A. Kongasseri, B. Chandra Garain, S. K. Pati and S. J. George, *Chem. Sci.*, 2022, **13**, 10011–10019.
41 A. A. Kongasseri, S. N. Ansari, S. Garain, S. M. Wagalgave and S. J. George, *Chem. Sci.*, 2023, **14**, 12548–12553.
42 N. Xue, H.-Y. Zhou, Y. Han, M. Li, H.-Y. Lu and C.-F. Chen, *Nat. Commun.*, 2024, **15**, 1425.
43 A. A. Kongasseri, S. Garain, S. N. Ansari, B. C. Garain, S. M. Wagalgave, U. Singh, S. K. Pati and S. J. George, *Chem. Mater.*, 2023, **35**, 7781–7788.
44 H. A. Duong, S. Chua, P. B. Huleatt and C. L. L. Chai, *J. Org. Chem.*, 2008, **73**, 9177–9180.
45 A. Ilina, K. E. Thorn, P. A. Hume, I. Wagner, R. R. Tamming, J. J. Sutton, K. C. Gordon, S. K. Andreassend, K. Chen and J. M. Hodgkiss, *Proc. Natl. Acad. Sci. U. S. A.*, 2022, **119**, e2212343119.
46 K. Vinod, S. D. Jadhav and M. Hariharan, *Chem. Eur. J.*, 2024, **30**, e202400499.
47 D. Sasikumar, K. Vinod, J. Sunny and M. Hariharan, *Chem. Sci.*, 2022, **13**, 2331–2338.
48 K. Vinod, R. Mathew, C. Jandl, B. Thomas and M. Hariharan, *Chem. Sci.*, 2024, **15**, 16015–16024.
49 I. Kaur, W. Jia, R. P. Kopreski, S. Selvarasah, M. R. Dokmeci, C. Pramanik, N. E. McGruer and G. P. Miller, *J. Am. Chem. Soc.*, 2008, **130**, 16274–16286.
50 K. Vinod, L. Hakeem K, D. Thomas, P. P. Das and M. Hariharan, *Org. Chem. Front.*, 2025, **12**, 33–41.
51 F. Ma, S. Zhang, J. Jiang, Y. Liu, J. Sun, J. W. Y. Lam, Z. Zhao and B. Z. Tang, *Adv. Mater.*, 2025, **37**, 2414188.
52 N. J. Hestand and F. C. Spano, *Acc. Chem. Res.*, 2017, **50**, 341–350.
53 B. Jeziorski, R. Moszynski and K. Szalewicz, *Chem. Rev.*, 1994, **94**, 1887–1930.
54 G. Tasi, I. Palinko, L. Nyerges, P. Fejes and H. Foerster, *J. Chem. Inf. Comput. Sci.*, 1993, **33**, 296–299.
55 J. Contreras-García, E. R. Johnson, S. Keinan, R. Chaudret, J.-P. Piquemal, D. N. Beratan and W. Yang, *J. Chem. Theory Comput.*, 2011, **7**, 625–632.
56 W. Zhang, S. Li, Y. Gong, J. Zhang, Y. Zhou, J. Kong, H. Fu and M. Zhou, *Angew. Chem., Int. Ed.*, 2024, **63**, e202404978.
57 J. Matern, N. Bäumer and G. Fernández, *J. Am. Chem. Soc.*, 2021, **143**, 7164–7175.
58 A. D. Nidhankar, Goudappagouda, D. S. Mohana Kumari, S. K. Chaubey, R. Nayak, R. G. Gonnade, G. V. P. Kumar, R. Krishnan and S. S. Babu, *Angew. Chem., Int. Ed.*, 2020, **59**, 13079–13085.
59 K. Vinod, D. Thomas and M. Hariharan, *Chem. Sci.*, 2025, DOI: **10.1039/D5SC00920K**.
60 D. M. E. Freeman, A. J. Musser, J. M. Frost, H. L. Stern, A. K. Forster, K. J. Fallon, A. G. Rapidis, F. Cacialli, I. McCulloch, T. M. Clarke, R. H. Friend and H. Bronstein, *J. Am. Chem. Soc.*, 2017, **139**, 11073–11080.
61 K. R. Peinkofer, M. L. Williams, G. C. Mantel, B. T. Phelan, R. M. Young and M. R. Wasielewski, *J. Am. Chem. Soc.*, 2024, **146**, 34934–34942.
62 H. Imahori, Y. Kobori and H. Kaji, *Acc. Mater. Res.*, 2021, **2**, 501–514.
63 X. Zhao, A. A. Sukhanov, X. Jiang, J. Zhao and V. K. Voronkova, *J. Phys. Chem. Lett.*, 2022, **13**, 2533–2539.
64 F. Ema, M. Tanabe, S. Saito, T. Yoneda, K. Sugisaki, T. Tachikawa, S. Akimoto, S. Yamauchi, K. Sato, A. Osuka, T. Takui and Y. Kobori, *J. Phys. Chem. Lett.*, 2018, **9**, 2685–2690.
65 K. Higashi, T. Okamoto, N. Iwaya, E. Sakuda, C. W. M. Kay, T. Ikoma, M. Higashi and Y. Kobori, *Angew. Chem., Int. Ed.*, 2025, **64**, e202503846.
66 P. K. Samanta, D. Kim, V. Coropceanu and J.-L. Brédas, *J. Am. Chem. Soc.*, 2017, **139**, 4042–4051.
67 Q. Zhang, J. Li, K. Shizu, S. Huang, S. Hirata, H. Miyazaki and C. Adachi, *J. Am. Chem. Soc.*, 2012, **134**, 14706–14709.
68 N. J. Hestand and F. C. Spano, *Chem. Rev.*, 2018, **118**, 7069–7163.
69 D. Chen, L. Zhang, T. Matulaitis, D. B. Cordes, A. M. Z. Slawin, X.-H. Zhang, I. D. W. Samuel and E. Zysman-Colman, *J. Mater. Chem. C*, 2023, **11**, 13095–13105.
70 M. K. Etherington, J. Gibson, H. F. Higginbotham, T. J. Penfold and A. P. Monkman, *Nat. Commun.*, 2016, **7**, 13680.
71 J. Li, T. Tian, D. Guo, T. Li, M. Zhang and H. Zhang, *J. Mater. Chem. C*, 2023, **11**, 6119–6129.
72 P. Pander, R. Motyka, P. Zassowski, M. K. Etherington, D. Varsano, T. J. da Silva, M. J. Caldas, P. Data and A. P. Monkman, *J. Phys. Chem. C*, 2018, **122**, 23934–23942.
73 S. Gelin, A. Champagne-Ruel and N. Mousseau, *Nat. Commun.*, 2020, **11**, 3977.